ACS APPLIED ENERGY MATERIALS

www.acsaem.org
Article

Saturating the Matrix: Nanocomposite Solution-Processed Sodium Aluminophosphate Solid Electrolytes

Thomas E. Gill, Guillaume Matthews, Yaoguang Song, Mo El Maoued, Adam J. Lovett, Sadia Sheraz, Nicholas P. Lockyer, Amita Ummadisingu, Thomas S. Miller, and Alexander J. E. Rettie*

Cite This: ACS Appl. Energy Mater. 2025, 8, 14592−14600
Read Online

ACCESS | Metrics & More | Article Recommendations | Supporting Information

ABSTRACT: Amorphous lithium solid electrolytes (SE) have enabled high performance lithium metal batteries, but sodium analogues are underexplored. Here, we report sodium aluminophosphate (NAPO) SEs synthesized via spin coating from aqueous solutions. Continuous, smooth, films with submicron thickness are produced after a mild annealing step. Exploration of the Na−Al−P−O phase space reveals nanocomposite materials comprising of an amorphous NAPO with crystalline $NaNO_3$ domains, suggesting a Na^+ saturation limit within the Al−P−O matrix. A maximum ionic conductivity of ≈10^{-8} S cm^{-1} is achieved, with the presence of the insulating $NaNO_3$ precursor necessary for high ionic conductivity. Electron microscopy, time-of-flight secondary ion mass spectrometry and optical measurements reveal that at low concentrations the $NaNO_3$ phase is initially present as diffuse nanoparticle domains and at higher concentrations it forms isolated micron-sized particles. The optimal NAPO SE has an activation energy of 0.80(1) eV, a moderate reduced Young's modulus ≈30 GPa and low electronic conductivity (≈10^{-14} S cm^{-1}), making these materials promising candidates for artificial solid electrolyte interphases or as solid electrolytes in sodium metal batteries.

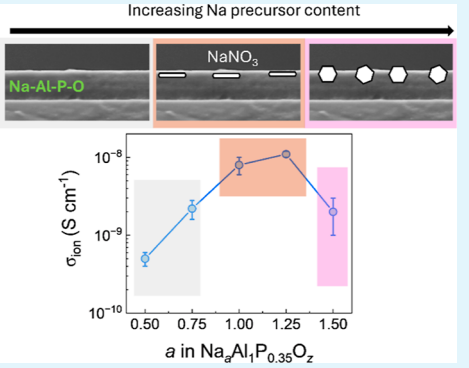

KEYWORDS: *nanocomposite, amorphous, solid electrolyte, thin film, scalable*

1. INTRODUCTION

Sodium-ion batteries (SIB) represent a promising alternative to lithium-ion batteries, due to the relative abundance and low-cost of sodium-based raw materials. However, the inherent reduction in energy density is a major drawback to the performance of SIBs. Integration of a Na metal anode (NMA) represents an avenue to maximize energy density, owing to its superior theoretic capacity versus commonly used hard carbon anodes (1166 vs 335 mAh g^{-1}).[1] However, the growth of metallic filaments (dendrites) during cycling poses a safety concern when integrating a NMA into cells with a flammable liquid electrolyte.

In light of this, there has been extensive research into crystalline sodium solid electrolytes (SEs) with ionic conductivities comparable to liquid counterparts.[2] Despite their mechanical toughness, Na SEs are susceptible to penetration by Na metal filaments that lead to cell failure.[3] There are notable exceptions to this, for example, Tsai et al.[4] reported a $Na_{3.4}Zr_2(SiO_4)_{2.4}(PO_4)_{0.6}$ (NZSP) solid electrolyte that demonstrated excellent dendrite inhibition, without any postprocessing or applied pressure. In contrast, several other reports claim that untreated NZSP-type SEs suffer from dendrite induced failure at low currents,[5−7] implying a complex relationship between SE properties and dendrite growth. Postprocessing of sodium-β''-alumina has also been reported to enable dendrite tolerance at high current densities.[8] However, this was achieved with a high temperature (900 °C) treatment step in an inert atmosphere, which is undesirable for large scale production.

The amorphous thin-film SE, lithium phosphorus oxynitride (LiPON) has been reported to exhibit stable Li plating/stripping for 10,000 cycles,[9] as well as high-rate capabilities (>10 mA cm^{-2}) when utilized in thin-film microbatteries.[10] This excellent tolerance to dendrite growth has been linked to key properties such as a low electronic conductivity,[11] as well as the absence of grain boundaries in the amorphous thin film.[12] LiPON has also been reported to produce a stable and low impedance interphase when in contact with Li metal.[13] Owing to these properties, LiPON has been studied as a stabilizing interfacial layer or artificial solid-electrolyte-interphase—increasing the dendrite tolerance of fast ion conducting SEs,[14,15] as well as improving the cyclability of Li metal full cells with liquid electrolytes.[16,17]

These reports prompted the development of sodium phosphorus oxynitride (NaPON), which was recently shown

Received: July 25, 2025
Revised: September 16, 2025
Accepted: September 17, 2025
Published: October 1, 2025

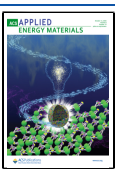

to be electrochemically stable against a NMA.[18−20] The major drawback of both LiPON and NaPON is the reliance on slow and expensive vacuum deposition techniques, which restricts their scalability and applicability to large-format cells. The development of amorphous Na thin-film SEs synthesized via scalable processing is therefore of significant interest. Previous work[21,22] has demonstrated that spin-coating inorganic nanoclusters from aqueous solutions with a mild annealing step (<500 °C) can yield smooth, dense, homogeneous Li-based films with desirable SE properties. Inspired by these studies, we report the synthesis of Na−Al−P−O (NAPO) thin film SEs. Avoiding the use of organic solvents is desirable to reduce costs and improve the sustainability of the manufacturing process.

First, we synthesize new NAPO thin film SEs and measure their physical, mechanical, structural and ionic conduction properties. Second, we explore the Na−Al−P−O phase space, revealing the presence of a two-phase system, comprising $NaNO_3$ crystallites embedded in an amorphous NAPO matrix. A maximum room temperature ionic conductivity of $\approx 10^{-8}$ S cm^{-1} is determined for some of these nanocomposites. The optimal composition has desirable mechanical and electronic properties for use as a thin solid electrolyte coating in advanced batteries.

2. EXPERIMENTAL METHODS

2.1. Material Preparation. NAPO thin films were prepared via spin coating from aqueous solutions. In a typical synthesis, precursor solutions were prepared by completely dissolving 25 mmol of $Al(OH)_3{\cdot}xH_2O$ (>99%, Thermo Fisher Scientific) in 20 mL of deionized (DI, 18 MΩ) water. The level of hydration was determined to be $x = 0.9$ via thermogravimetric analysis. To these solutions, 37.5 mmol of HNO_3 (70% aq, >99.9%, Sigma-Aldrich) and 12.5 mmol of H_3PO_4 (85% aq, >99.9%, Sigma-Aldrich) were added and stirred overnight at 80 °C to allow complete dissolution. After cooling to room temperature, 25 mmol of $NaNO_3$ (>99%, Fisher Scientific) was added and stirred at 50 °C for 24 h. The $NaNO_3$ and H_3PO_4 amounts were adjusted in order to obtain a range of compositions with various Na/Al/P molar ratios. Finally, all solutions were diluted with DI water to achieve a final concentration of 0.8 M with respect to Al.

Silicon (Si) wafers (p-type, ⟨100⟩, boron-doped, single-side polished, resistivity <0.01 Ω cm, PI-KEM) were used as a substrate and bottom electrode. The Si substrates were cut into 2 × 2 cm^2 samples with a diamond scribe, and ultrasonicated in a series of acetone, IPA and DI water, before being dried under nitrogen. To remove any remaining surface contaminants the substrates were O_2 plasma-treated (Henniker HPT-100) at 100 W for 5 min, resulting in a clean hydrophilic surface.

The precursor solution was then sonicated at 50 °C for 30 min. Once cooled to room temperature, the substrate was flooded with solution through a 0.2 μm Teflon filter attached to a syringe, spin coated at 3000 rpm for 30 s and immediately transferred to a preheated hot plate at 275 °C for 5 min. After removing the samples and allowing them to cool to room temperature, the process was repeated to obtain multilayer films. Unless stated otherwise, 2 layers were deposited for characterization studies. Once the final layer was deposited, a final 1 h anneal was conducted either at 275 °C using a hot plate or at 350−800 °C in a box furnace. All films were stored in an Ar-filled glovebox (H_2O and O_2 level <0.5 ppm) to minimize any contamination with atmospheric moisture.

A $NaNO_3$ pellet (12 mm diameter, 5 mm thick) was prepared by placing vacuum-dried $NaNO_3$ powder into a cylindrical pressing die and pressed with a uniaxial pressure ≈100 MPa at room temperature. The pellet was then calcinated at 275 °C for 1 h in air in a box furnace before being vacuum-dried overnight at 100 °C and stored in an Ar-filled glovebox.

2.2. Physicochemical Characterization. Film thickness was determined using a SEMILAB SE-2000 rotating compensator spectroscopic ellipsometer. Films deposited on Si substrates were measured under ambient conditions with an incident angle of 70° between 250 and 1700 nm wavelengths. The measured ellipsometry spectra (Figure S1 in the Supporting Information) were modeled and analyzed with the Cauchy dispersion law using Semilab SEA software to obtain the film thickness. Cross-sectional imaging was carried out using scanning electron microscopy (SEM, ZEISS, GeminiSEM 360). Samples for SEM were prepared by sputtering a thin layer of Au onto the surface, before being gently broken into <0.5 cm^2 pieces. The surface morphology and mechanical properties were characterized using atomic force microscopy (AFM). AFM experiments were carried out using a Bruker Dimensions Icon with ScanAsyst housed in an Ar-filled glovebox (<0.5 ppm of H_2O and O_2) with Bruker RTESPA-150 (Sb (n) doped Si with reflective Al coating, k = 5 N m^{-1}, f^0 = 150 kHz) or Bruker RTESPA-300 (Sb (n) doped Si with reflective Al coating, k = 40 N m^{-1}, f^0 = 200 kHz) AFM tips. Two modes were used. Bruker's ScanAsyst mode (peak force tapping) was used to characterize the film topography. The reduced Young's modulus was mapped using the Quantitate NanoMechanics (QNM) PeakForce tapping mode using the relative mode calibrated against highly ordered pyrolytic graphite (18 GPa).[23,24] Further information about the method can be found elsewhere.[25] All AFM images were analyzed using the Gwyddion software.[26]

Scanning-transmission electron microscopy (STEM) analysis was performed by using a Zeiss Merlin instrument equipped with a field emission gun (FEG) operated at 30 kV. Prior to analysis, a suspension was prepared by adding a few mg of NAPO powder into 15 mL of acetone in a beaker which was subsequently ultrasonicated for 2 min. A lacey carbon copper grid was dipped into the suspension and dried to make the STEM sample. NAPO powder was obtained by scratching a single-layer NAPO film deposited onto a glass microscope slide. STEM micrographs were acquired with bright field imaging mode, and a low acceleration voltage was required to avoid beam damage of the specimen.

Grazing incidence X-ray diffraction (GI-XRD) was conducted with a Malvern PANalytical Empyrean diffractometer, using a Cu source. Films were deposited onto fused silica substrates, which were cleaned in the same way as described for Si wafers in Section 2.1. The fused silica substrates (1 mm thick) were purchased precut to 2 × 2 cm^2 from Multilab. Data was collected with a fixed angle of incidence (1°) over a 2θ range of 10 to 50°.

Surface composition was determined using X-ray photoelectron spectroscopy (Thermo Fisher, Kα photoelectron spectrometer, Al source) with binding energies referenced against the adventitious carbon (C) 1s peak at 284.8 eV. The process was carried out under ultrahigh vacuum conditions (10^{-7} to 10^{-6} Pa). Survey scans were collected first before additional scans centered around regions containing elements of interest were conducted. In order to collect data with adequate signal-to-noise ratio, a minimum of 50 scans were used in the regions of Na, Al, P, O and N. CasaXPS software was used to analyze the data, and Shirley background fitting was used. An estimate of the surface-level elemental composition was determined from the peak areas, which were first normalized using the relative sensitivity factors from CasaXPS, Na (8.52), Al 2p (0.537), P 2p (1.192) and O 1s (2.93), and N 1s (1.8). Time of flight secondary ion mass spectrometry (ToF-SIMS) was conducted with an Ionoptika J105-SIMS instrument,[27] using a 40 keV C_{60}^+ primary ion beam in positive and negative ion imaging mode. Samples were first heated to 50 °C inside the ToF-SIMS instrument prior to analysis. Depth profile analysis was then completed using a primary ion dose of 1.11 × 10^{13} ions cm^{-2} per layer with 128 × 128 pixels over an area of 150 μm × 150 μm until a total dose of 1.5 × 10^{15} ions cm^{-2} was reached. Diffuse reflectance measurements were obtained using a Shimadzu UV-2600i spectrophotometer with an integrating sphere accessory, in a wavelength range of 220−1400 nm with a 1 nm step-size.

2.3. Electronic and Electrochemical Characterization. Through-plane ionic conductivity measurements were performed throughout. Circular Al top contacts (1.13 mm^2, ≈100 nm) were

https://doi.org/10.1021/acsaem.5c02284
ACS Appl. Energy Mater. 2025, 8, 14592−14600

deposited by sputtering through a shadow mask, and Al foil was adhered to the back of the Si wafers using conductive Ag epoxy (Agar Scientific). An in-house cell holder was used to take conductivity measurements, where an Au-plated screw with a rounded tip gently contacted the Al contacts. Since thinner films could be susceptible to piercing under contact pressure from the screw, 2-layer films were used. The Au screw and Al foil were connected to a potentiostat (Reference 600+, Gamry) for electrochemical measurements. For studying the ionic conductivity of the $NaNO_3$ pellet, a separate in-house cell was used, which consisted of two stainless steel pins connected in a PTFE holder which could be hand-pressed and screwed together to ensure good contact.[28] Electrochemical impedance spectroscopy (EIS) was conducted using a 20 mV perturbation voltage over a frequency range of 100 mHz to 1 MHz for NAPO films, with a lower limit of 0.1 mHz used for the $NaNO_3$ pellet. The EIS data were fit using an equivalent circuit model (ECM) consisting of a combination of electrical components in a Randles-type circuit.[29,30] A resistor (R) was used to model the impedance originating from electrical contacts (R_o), a constant phase element (CPE) accounted for electrode polarization due to nonsymmetric blocking electrodes (CPE_{pol}). A "*RCPE*" unit consisting of a R and CPE in parallel was used to represent the relaxation process associated with the migration of mobile ions through the bulk of the solid electrolyte. From this, a value for the bulk resistance (R_b) of the solid electrolyte could be estimated and the ionic conductivity, σ_{ion} calculated using eq 1

$$\sigma_{ion} = \frac{l}{R_b A} \tag{1}$$

where, l is the thickness of the film (as determined by ellipsometry), R_b is the bulk solid electrolyte resistance and A is the geometric area of the Al contact. An average was taken from 3 different films, with each film being sampled in multiple positions (>3) across the film. For the $NaNO_3$ pellet, l was determined with a digital Vernier caliper and A was defined by the area of the pellet. Room temperature measurements were conducted inside an Ar-filled glovebox. All EIS measurements were conducted within 24 h of film synthesis. However, repeat tests after 1 month of storage in an Ar-filled glovebox indicated no significant change to the resistance. Temperature-dependent EIS measurements were carried out inside a thermal chamber in air, with data collected at defined temperatures after a 30 min wait-time to ensure thermal equilibrium. By fitting the data to an Arrhenius relationship (eq 2), the activation energy (E_a) of the ion hopping process was determined

$$\sigma_{ion} T = \sigma_o \, e^{-E_a/kT} \tag{2}$$

where, σ_0 is a pre-exponential factor, E_a is the activation energy, k is the Boltzmann constant (8.62×10^{-5} eV K^{-1}), and T is temperature. For the DC polarization experiments, a voltage bias of 1 V was applied for 1 h and the current–voltage curve fit to an exponential decay function. A longer duration constant-voltage experiment was run over 12 h, which confirmed that 1 h was sufficient to reach steady state.

3. RESULTS AND DISCUSSION

3.1. Synthesis. In a previous study,[22] we reported a range of $Li_aAl_1P_cO_z$ thin films, with the nominal Li and P content in the precursor solution varied between $2.25 < a < 3.25$ and $1.15 < c < 1.5$. Attempts to incorporate Na^+ into similar Al–P–O frameworks by direct substitution of $NaNO_3$ for $LiNO_3$ in these precursor solutions resulted in films of poor quality by visual inspection. Modifying both the Na and P contents to molar ratios of Na/Al/P = 1:1:0.5 yielded visibly homogeneous thin films, indicating different interactions between Na and the Al–P–O networks compared to Li. Annealing similarly deposited thin films at 275 °C for 1 h has been shown to be sufficient to dehydrate, condense and decompose Li–Al–P–O and Al–P–O phases deposited via spin coating from aqueous solutions.[21,22,31] This is lower than the known decomposition temperature of pure lithium nitrate (640 °C),[32] demonstrating lower thermal requirements for thin films compared to bulk powders. Therefore, despite the relatively higher decomposition temperature of pure $NaNO_3$ (740 °C),[32] a 275 °C annealing temperature was used to produce Na–Al–P–O (NAPO) thin films as well.

3.2. Physicochemical & Electrochemical Properties. First, the cross-sectional morphology of the deposited films was observed by SEM. From Figure 1a, the 7-layer film appears

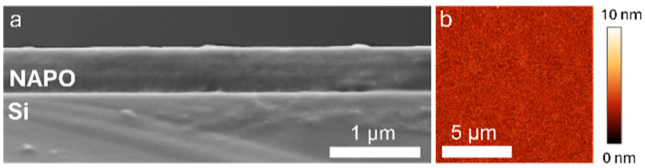

Figure 1. (a) Cross-sectional SEM image of a 7-layer $Na_1Al_1P_{0.5}O_z$ film on a Si substrate annealed at 275 °C. (b) AFM surface topography map of a 2-layer $Na_1Al_1P_{0.5}O_z$ film.

uniform and dense, with no clear signs of cracks or pinholes. The thickness determined from the SEM image was ≈500 nm for the 7-layer film, which was in good agreement with the thickness determined via ellipsometry (505 nm). Ellipsometry studies on 2-layer films revealed a thickness of 160 nm, indicating a thickness of ≈80 nm per layer. The surface topography of the deposited films was then studied with AFM (Figure 1b). The films were flat and continuous, with a low average surface roughness ≤1 nm. The reduced Young's modulus was determined from quantitative nanomechanical AFM to be 28.1 GPa. This value is lower than LiPON (77 GPa),[33] LAPO (42 GPa)[22] and garnet oxides (140–160 GPa),[34] and above typical sulfides (15–20 GPa).[35,36] The value for NAPO calculated here is promising, as an intermediate Young's modulus is considered important for the dendrite tolerance of LiPON.[33]

The surface chemical composition was then studied using X-ray photoelectron spectroscopy (XPS). The Na 1s, O 1s, Al 2p and P 2p spectra (Figure 2) for a film annealed at 275 °C showed the elements in their expected charge states of Na^+, O^{2-}, Al^{3+}, and P^{5+}. The N 1s spectra displayed a peak at around 407.5 eV, which is typical for N in a $NaNO_3$ environment, indicating there was a fraction of the precursor salt that remained undecomposed after the 275 °C annealing process. This was examined further in the Na 1s spectra which could be fit with two peaks: the largest peak at 1071.9 eV was assigned to the Na^+ in the NAPO matrix, with a secondary peak at 1070.4 eV assigned to Na^+ in a $NaNO_3$ environment. A normalized area ratio of ≈1:1 was determined for the $NaNO_3$ peaks in the N 1s and Na 1s spectra, consistent with the elemental ratio N in $NaNO_3$. Comparison of the peak areas between the two Na features indicated ≈10% of Na existed as $NaNO_3$. The O 1s spectra contained a dominant peak at 531.4 eV which is characteristic of O within an $AlPO_4$-type environment, with the higher energy peak at 536.6 eV associated with an Na Auger emission. There were also no clear indications of peaks associated with H_2O (≈533 eV) or –OH (≈532 eV) groups, suggesting that NAPO is largely dehydrated after annealing, consistent with the previous reports on LAPO thin films synthesized via spin coating from aqueous solutions.[21,22] The Al 2p and P 2p peaks at 74.5

https://doi.org/10.1021/acsaem.5c02284
ACS Appl. Energy Mater. 2025, 8, 14592–14600

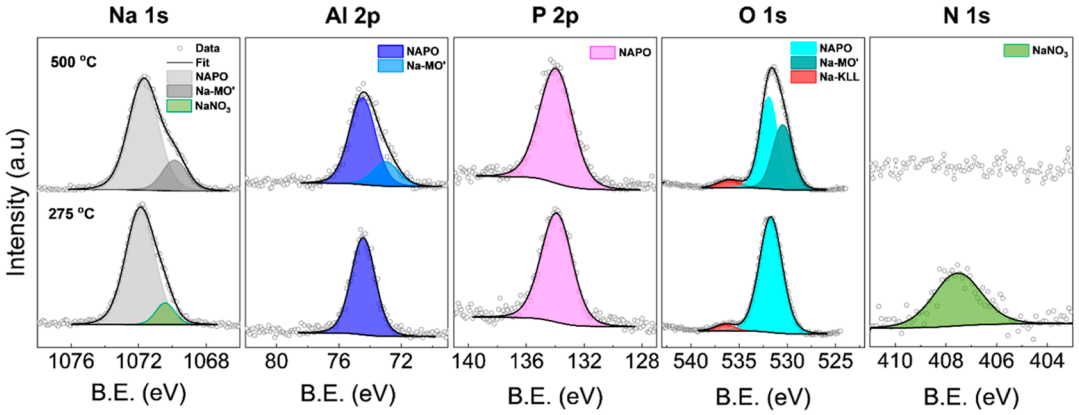

Figure 2. XPS data for $Na_1Al_1P_{0.5}O_z$ films after a 1 h anneal at 275 and 500 °C.

and 133.8 eV respectively are consistent with an $AlPO_4$-type environment.

Preliminary experiments showed that the residual nitrate on the surface could be removed by increasing the final annealing temperature to 500 °C, as shown by the absence of the nitrate peak in the N 1s spectra. However, a different lower energy Na peak was observed in the Na 1s spectra, indicating the formation of a new secondary Na environment. The emergence of a secondary peak in the O 1s indicated the presence of separate oxide framework (Na-MO′), and a new shoulder peak in the Al 2p spectra indicated that a fraction of the Al^+ is also integrated into this Na-MO′ structure. There were no new environments observed in the P 2p spectra, with the minor shifts in binding energy related to the change in the neighboring chemical environment after the removal of the residual nitrate. It is worth noting that an immediate 5 min cure at 275 °C was used prior to the final 1 h anneal at 500 °C. Therefore, this separate phase is likely a result of a secondary reaction that occurs during the 500 °C anneal, where the residual nitrate present after the preset anneal at 275 °C is decomposed into a new environment within the film. The surface elemental ratios determined via XPS (Table S1, Supporting Information) showed that the elemental Na and P content was consistent between different annealing temperatures.

The structural properties of films annealed at 275 and 500 °C were assessed using GI-XRD (Figure 3a). The data collected for both films showed a predominantly amorphous structure, which is consistent with the reports on related Li-containing materials.[21,22] However, for the film annealed at 275 °C there was a weak peak around 29° which was indexed to crystalline $NaNO_3$ powder (data experimentally collected). The lack of this feature at 500 °C is consistent with the loss of the nitrate peak in the N 1s spectrum.

The ionic conductivity (σ_{ion}) of NAPO films annealed at 275 °C and 500 °C was determined using EIS. Although XPS showed no strong peaks associated with H_2O or −OH, measures were taken to minimize any potential impact of water contamination due to hygroscopic nature of $NaNO_3$. All films were immediately transferred from hot plate to a vacuum chamber to apply the Al electrodes. Samples were then heated at 150 °C for 1 h during the drying of Al back contacts before immediate transfer inside an Ar-filled glovebox for testing.

EIS data (Figure 3b) collected for both samples were adequately fit by the ECM shown inset in Figure 3b. A singular "*RCPE*" unit was used to model the conduction of Na^+. This

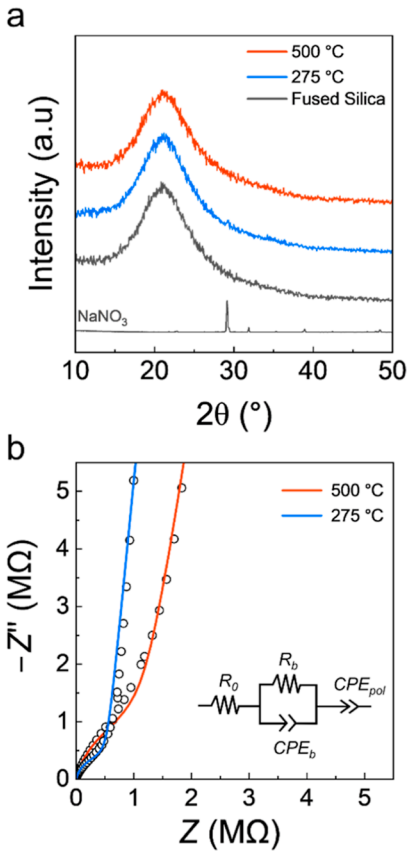

Figure 3. (a) GI-XRD data collected for NAPO films annealed at 275 and 500 °C, and $NaNO_3$ precursor. (b) EIS data for NAPO films annealed 275 and 500 °C with equivalent circuit model used to fit the data.

choice was supported by the presence of a singular peak in the Bode plots for both films (Figure S2 in the Supporting Information), indicating the presence of a single charge transfer process. As the annealing temperature increased from 275 to 500 °C, there was a small reduction in the ionic conductivity from $2.3(3) \times 10^{-9}$ to $1.3(2) \times 10^{-9}$ S cm^{-1}. This agrees with previous work on a LAPO material, in which an inverse relationship between σ_{ion} and annealing temperature was observed.[22]

To understand the potential impact of the residual $NaNO_3$ on the ionic conductivity, EIS data was also collected for a vacuum-dried $NaNO_3$ pellet (Figure S3 in the Supporting

https://doi.org/10.1021/acsaem.5c02284
ACS Appl. Energy Mater. 2025, 8, 14592−14600

Information). It should be noted that an elevated temperature of 40 °C was required to obtain meaningful data in this case. The bulk σ_{ion} was $\approx 10^{-11}$ S cm^{-1} at 40 °C, 2 orders of magnitude slower than the value reported for the two-phase $Na_1Al_1P_{0.5}O_z$ at room temperature. The higher σ_{ion} in the two-phase system despite the presence of insulating crystalline $NaNO_3$ suggests that such particles may be beneficial to the conduction properties of the film. However, it is also possible the $NaNO_3$ crystallites are isolated within the NAPO matrix and are not involved in the charge transport. Furthermore, the reduction in the σ_{ion} despite its removal at 500 °C may also be connected to structural changes that occur at the higher annealing temperature, causing less favorable pathways for ionic conduction.

3.3. Compositional Exploration. Variation of elemental composition has been shown to impact both ion transport and structural properties of bulk sodium aluminophosphate glasses.[37,38] Therefore, a systematic exploration of the NAPO phase space was conducted in order to further study the two-phase systems observed in Section 3.2. This was achieved by adjusting the Na and P ratios relative to Al in $Na_aAl_1P_cO_z$ while keeping the annealing temperature constant at 275 °C. Note that a and c represent the nominal Na and P content in the precursor solutions. First, fixing the Na content at $a = 1$, the P content in $Na_1Al_1P_cO_z$ films was varied between $0.2 < c < 1.0$. The analysis of the collected N 1s XPS spectra revealed a complete loss of the nitrate peak as P content was increased to $c = 1.0$. The GI-XRD data (Figure 4b) displays a

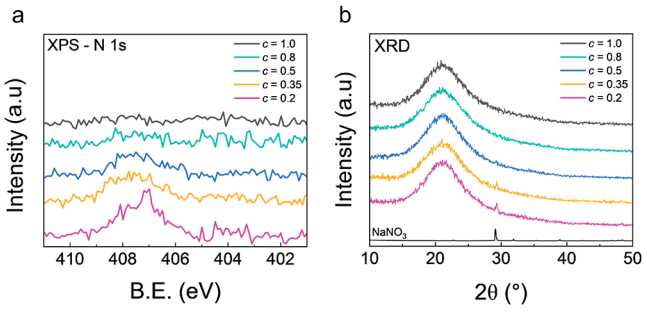

Figure 4. (a) N1 XPS spectra, (b) GI-XRD data for $Na_1Al_1P_cO_z$ films with varied P content from $0.2 < c < 1.0$ and a fixed annealing temperature of 275 °C.

predominantly amorphous framework for all NAPO phases, with the presence of crystalline $NaNO_3$ evident for phases $c \leq 0.5$. The increased peak intensity for $c \leq 0.35$ suggests a greater presence of $NaNO_3$ crystallites within these NAPO matrices. From the XPS and XRD data for $c \geq 0.8$ it is apparent that a 275 °C anneal was sufficient to achieve extensive, if not complete, decomposition of $NaNO_3$. Therefore, it can be inferred that for $c < 0.8$ the Al−P_c−O_z matrices are likely saturated with Na^+ ions, and the excess crystallized out in the form of $NaNO_3$. From the fitted EIS data (Figure S4, Supporting Information) the σ_{ion} (Figure 5) was shown to increase from $1.5(6) \times 10^{-10}$ S cm^{-1} to $8(2) \times 10^{-9}$ S cm^{-1} as the P content was reduced from $c = 1.0$ to 0.35, before decreasing to $4(1) \times 10^{-9}$ S cm^{-1} at $c = 0.2$. A maximum σ_{ion} was achieved for a composition of $Na_1Al_1P_{0.35}O_z$, which consisted of an amorphous NAPO phase and crystalline $NaNO_3$ phase. Since this σ_{ion} value is ~3 orders of magnitude higher than the calculated bulk σ_{ion} for $NaNO_3$, we assume that the $NaNO_3$ crystallites are likely isolated within the more

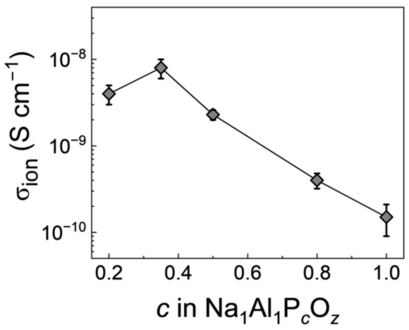

Figure 5. Room temperature σ_{ion} with error bars calculated using ±1 standard deviation. A final annealing temperature of 275 °C was used for all films.

conductive amorphous NAPO matrix. This indicates that for improved ionic conductivity it was desirable to saturate the NAPO matrix to the point that $NaNO_3$ crystallites appear in the materials.

To explore this further, we fixed the P content at $c = 0.35$ and 0.8 and then varied the Na content in the $Na_aAl_1P_{0.35}O_z$ and $Na_aAl_1P_{0.8}O_z$ films between $0.5 < a < 1.5$ and $1.0 < a < 2.5$ respectively. The GI-XRD data (Figure 6a) demonstrated an

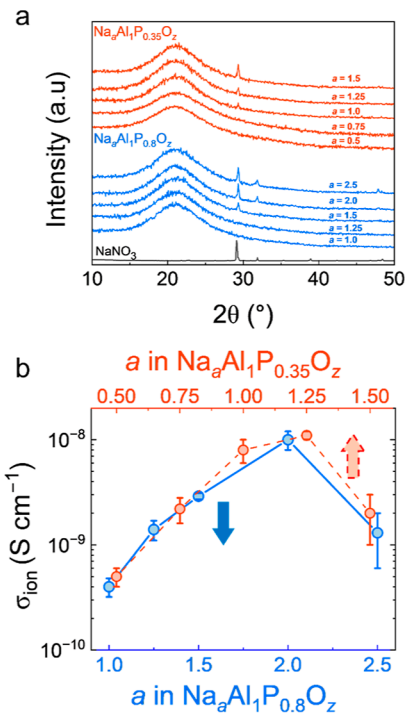

Figure 6. (a) GI-XRD data for $Na_aAl_1P_cO_z$ films with fixed P values (c = 0.35 and 0.8) and varied Na values. (b) Calculated room temperature σ_{ion} values for the various NAPO compositions, with error bars calculated using ±1 standard deviation. A final annealing temperature of 275 °C was used for all films.

absence of the $NaNO_3$ peaks at Na content, $a = 0.5$ and 0.75 (P = 0.35, red) and $a = 1.0$ and 1.25 (P = 0.8, blue), indicating complete integration of the Na^+ ions from the $NaNO_3$ precursor into amorphous $Na_{0.5-0.75}Al_1P_{0.35}O_z$ and $Na_{1.0-1.25}AlP_{0.8}O_z$ matrices. Increasing the Na content to a = 1.0 (P = 0.35) and a = 1.5 (P = 0.8) results in the emergence of crystalline $NaNO_3$ peaks, indicating matrix saturation. When the Na content is further increased to a = 1.25 and 1.5 (c =

https://doi.org/10.1021/acsaem.5c02284
ACS Appl. Energy Mater. 2025, 8, 14592−14600

0.35), and a = 2.0 and 2.5 (c = 0.8), increased XRD peak intensities, along with the emergence of additional peaks consistent with $NaNO_3$ at 32° and 48° were observed. Comparison between the GI-XRD data sets suggests a clear link between the P content (c) in the precursor solution and the amount of Na (a) that can be integrated into the Al−P_c−O_z matrices. Figure 6b displays the σ_{ion} determined from the fitted EIS data collected for all compositions. The σ_{ion} for $Na_aAl_1P_{0.35}O_z$ films increased from to $5(1) \times 10^{-10}$ S cm^{-1} to $1.1(1) \times 10^{-8}$ S cm^{-1} as the Na content was increased from a = 0.5 to 1.25, with a subsequent decrease to $2(1) \times 10^{-9}$ S cm^{-1} at a = 1.5. Similarly, the σ_{ion} for $Na_aAl_1P_{0.8}O_z$ films increased from $4.0(8) \times 10^{-10}$ S cm^{-1} to $1.0(2) \times 10^{-8}$ S cm^{-1} as the Na content was increased from a = 1.0 to 2.0, with a reduction to $1.3(7) \times 10^{-9}$ S cm^{-1} at a = 2.5. For both systems, an optimum $\sigma_{ion} \approx 10^{-8}$ S cm^{-1} was achieved by increasing the concentration of the $NaNO_3$ content in the precursor solutions past the point of the matrix saturation, indicating that to some extent, the addition of an ionically insulating $NaNO_3$ phase is beneficial to the σ_{ion}.

3.4. Nanocomposite Structure. To gain information on the structure of the nanocomposites, STEM was conducted on powder scratched from a $Na_{2.5}Al_1P_{0.8}O_z$ film. The bright-field image (Figure 7) displays multiple, dark, highly diffracting

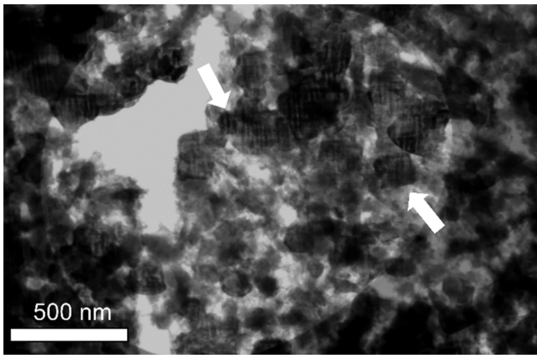

Figure 7. STEM bright-field image of $Na_{2.5}Al_1P_{0.8}O_z$. The white arrows indicate crystalline domains.

(crystalline) nanoparticles (50−200 nm) embedded in a transparent (amorphous) matrix. Together, with the GI-XRD data this is consistent with crystalline $NaNO_3$ nanoparticles dispersed within an amorphous NAPO matrix.

ToF-SIMS 3D analysis was then conducted on 4-layer films with the compositions $Na_{0.5}Al_1P_{0.35}O_z$, $Na_{1.0}Al_1P_{0.35}O_z$, and $Na_{1.5}Al_1P_{0.35}O_z$ (Figure 8). The collected secondary ions showed a uniform distribution of Na^+, Al^+ and PO_3^- throughout all films, representing the homogeneous NAPO matrix. The depth profiles and 2D area maps for collected NO_3^- ions for all 3 samples are displayed in Figure 8a,b, together with PO_3^- ions for comparison. The presence of $NaNO_3$ was indicated by the presence of NO_3^- ions. It is noted that the entire film thickness was sputtered through after an ion dose of 3×10^{15} ions cm^{-2}, but analyses was limited to 1.5×10^{15} ions cm^{-2} to allow for data collection in a reasonable time frame. For the $Na_{0.5}Al_1P_{0.35}O_z$ sample, there was some presence of NO_3^- in the spectrum, however this was limited to the top surface. When increasing the Na content to $Na_{1.0}Al_1P_{0.35}O_z$, a higher intensity of NO_3^- ions was observed at the top surface, which reduced quickly within the bulk of the films. The 2D area map displayed domains rich in NO_3^- that

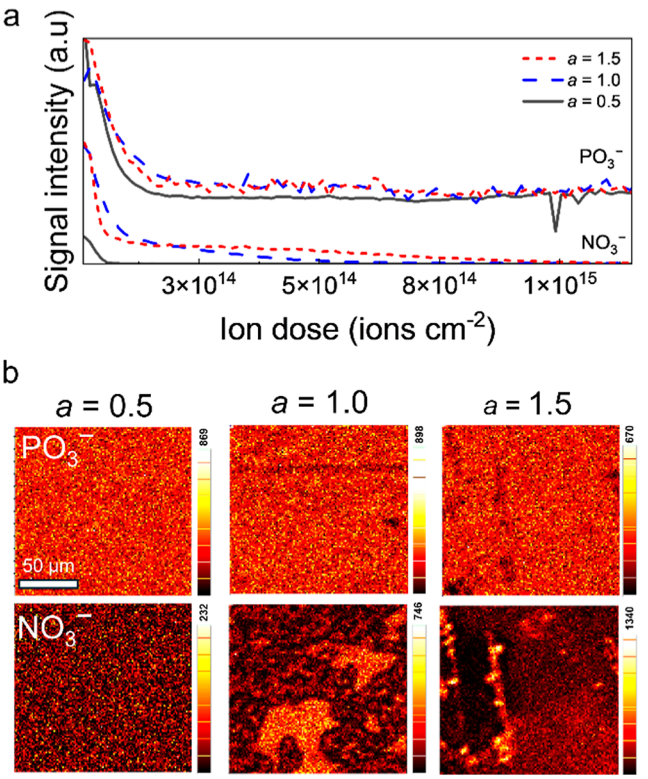

Figure 8. ToF-SIMS (a) depth profiles and (b) primary layer 2D area maps of secondary NO_3^- and PO_3^- ions $Na_aAl_1P_{0.35}O_z$ films with varied a content. An intensity scale with the maximum count level is shown for each 2D area map.

were 10−50 μm in size. The primary ion beam, C_{60}^+ used for ToF-SIMS analysis was focused to ≈2 μm, which impacted the ability to distinguish particles smaller than this, however this is consistent with these areas being rich in $NaNO_3$ nanoparticles. Upon increasing the Na content to $Na_{1.5}Al_1P_{0.35}O_z$, an increased presence of NO_3^- was evident in the depth profiles, which showed a higher intensity of NO_3^- ions that become negligible after about one-third of the film thickness. The 2D maps show ≈10 μm particles which are randomly distributed and separated across the material's surface.

Taken altogether, the GI-XRD, STEM and ToF-SIMS data suggest that as the $NaNO_3$ begins to crystallize out of the amorphous matrix, it starts as small particles which group together in relatively large domains in close proximity to the film surface. Upon further increase of the $NaNO_3$ content, there is a preference for the crystals to group together in isolated clusters—likely made up of ≈100 nm size crystals as indicated by the STEM analysis. These clusters are embedded at the materials surface and extend further down into the bulk. These are displayed in the 3D volume maps generated from the ToF-SIMS data (Figure S5, Supporting Information).

The optical properties of the materials were also measured via diffuse reflectance analysis (Figure 9). The dip in reflectance near 400 nm is due to light absorption by $NaNO_3$, which has been reported to have a band gap close to 3 eV.[39] As the Na content in $Na_aAl_1P_{0.35}O_z$ films was increased from a = 0.5 to 1.25, the increasing surface coverage by uniformly distributed $NaNO_3$ crystals results in greater surface roughness. This causes the observed increase in diffuse reflectance for these samples. When a = 1.5, the low-wavelength reflectance peak experiences a sudden drop in

https://doi.org/10.1021/acsaem.5c02284
ACS Appl. Energy Mater. 2025, 8, 14592−14600

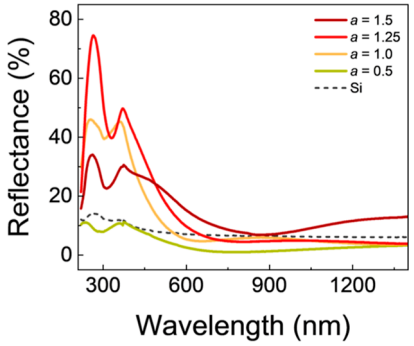

Figure 9. Reflectance data for $Na_aAl_1P_{0.35}O_z$ films with varied a content, together with Si substrate for reference.

intensity. We propose that at the highest concentration of $NaNO_3$, the aggregation of crystals into fewer isolated clusters smoothens the surface on average. This results in more specular behavior and a reduced diffuse scattering of incoming light. The increase in reflectance observed at higher wavelengths is due to the deeper extension of these clusters into the bulk of the material, where infrared radiation is more penetrative than visible and UV light.

Returning to the trends of σ_{ion}, in the oversaturated two-phase $Na_{1.5}Al_1P_{0.35}O_z$ material, the extensive presence of the 10 μm $NaNO_3$ particles negatively impacts the σ_{ion}. On the other hand, in an intermediate-two phase system the NAPO matrix is saturated with Na^+ ions, and the reduced concentration of the insulating $NaNO_3$ phase (dispersed in subsurface domains) has a limited impact on σ_{ion}. However, the addition of ionically insulating particles (e.g., SiO_2 or Al_2O_3) has been reported to enhance the σ_{ion} when integrated into composites with numerous crystalline ion conductors.[40] The exact reason for improved σ_{ion} is unknown but could be due to favorable changes in the crystal structure, lattice defects, and enhanced conduction pathways along a matrix−particle interface created by the dispersion of this second phase. The enhanced σ_{ion} observed in this work may therefore also be a result of these favorable pathways formed by the $NaNO_3$ particles. However, it could also be due to formation of an ideal Na−Al−P−O composition that just happens to exsolve $NaNO_3$. Future work will look to better understand the underlying mechanism.

For the materials with strong XRD peaks for $NaNO_3$ ($Na_{1.25-1.5}Al_1P_{0.35}O_z$ and $Na_{2.0-2.5}Al_1P_{0.8}O_z$), visual color changes during prolonged exposure to ambient air indicated moisture contamination. The high content of $NaNO_3$ in these materials will likely lead to increased moisture sensitivity, making them tougher to process and handle in ambient air. Therefore, the optimum composition was selected as $Na_1Al_1P_{0.35}O_z$, with an σ_{ion} = 8(2) × 10^{-9} S cm^{-1}. Surface studies with AFM were reconducted (Figure S6, Supporting Information), demonstrating a low average roughness (<1 nm), and a reduced Young's modulus of ≈30 GPa. For the subsequent charge transport investigations, this composition was chosen, and unless stated otherwise, the abbreviation NAPO will refer to the composition $Na_1Al_1P_{0.35}O_z$ annealed at 275 °C.

3.5. Activation Energy Analysis. The activation energy (E_a) of the ion conduction process was calculated for optimized NAPO as 0.80(1) eV, using an Arrhenius relationship (Figure 10). This value is larger than values reported for LiPON (0.55 eV)[41] and NaPON (0.53 eV),[18] which is unsurprising given the comparatively lower σ_{ion} (NAPO ≈10^{-8} S cm^{-1}, LiPON ≈10^{-6} S cm^{-1}, NaPON ≈10^{-7} S cm^{-1}). This value is greater than the value reported for a bulk sodium aluminophosphate glass (0.67 eV),[37] however, a σ_{ion} value of ≈10^{-8} S cm^{-1} was achieved only at an elevated temperature (75 °C), at which NAPO demonstrated a superior σ_{ion} = 1.5 × 10^{-7} S cm^{-1} (70 °C). The comparatively higher ionic conductivity, despite the greater activation energy, could be explained by an increased concentration of mobile Na^+ ions within the NAPO material.

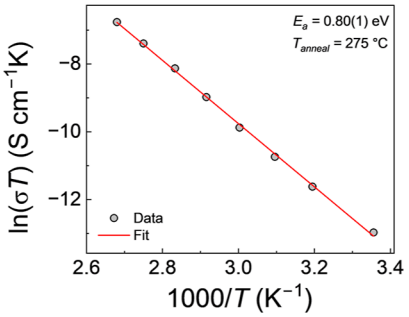

Figure 10. Temperature dependent σ_{ion} measurements from 25 to 100 °C. Calculated E_a inset, with error determined from the standard error as reported by the Origin fitting software.

3.6. Electronic Conductivity. Low bulk electronic conductivities have been shown to play an important role in resisting growth of alkali metal dendrites, and enabling stable plating and stripping of Li for example.[11] From the steady-state current value of a voltage decay curve (Figure 11) the electronic conductivity of the NAPO film was calculated as ≈10^{-14} S cm^{-1}, which compares well to the values reported for LiPON and water-processed LAPO films (≈10^{-11} to 10^{-14} S cm^{-1}).[11,22] Therefore, these materials are promising as artificial solid electrolyte interfaces or as SEs in alkali metal batteries.

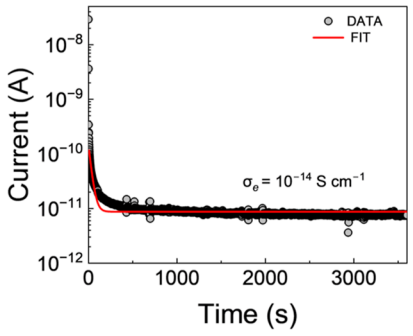

Figure 11. Current−voltage decay curve for the optimal NAPO film annealed at 275 °C.

4. CONCLUSIONS

Sodium thin film solid electrolytes were synthesized via spin coating from aqueous precursors. First, the physical, structural, and electrochemical properties were benchmarked using a $Na_1Al_1P_{0.5}O_z$ composition. A 275 °C anneal was sufficient to form continuous, dense thin films with low surface roughness (<1 nm) and a moderate Young's modulus. XPS and XRD analyses indicated the presence of residual $NaNO_3$ precursor salt which was decomposed after an 1 h anneal at 500 °C. The Na−Al−P−O phase space was then explored, which revealed the existence of two-phase compositions, made up of an amorphous NAPO phase and crystalline $NaNO_3$ precursor

https://doi.org/10.1021/acsaem.5c02284
ACS Appl. Energy Mater. 2025, 8, 14592−14600

domains. A maximum σ_{ion} of $\approx 10^{-8}$ S cm^{-1} was reported in three of these nanocomposites: $Na_1Al_1P_{0.35}O_z$, $Na_{1.25}Al_1P_{0.35}O_z$ and $Na_{2.0}Al_1P_{0.8}O_z$. Although the role of the insulating $NaNO_3$ crystallites on the σ_{ion} is not fully understood, it is clear that partially increasing their presence within the films is desirable. Temperature dependent σ_{ion} measurements for the $Na_1Al_1P_{0.35}O_z$ materials exhibited an activation energy of 0.80(1) eV and a low σ_e ($\approx 10^{-14}$ S cm^{-1}). These results should aid in designing new amorphous and amorphous-ceramic solid electrolytes for alkali metal batteries.

■ ASSOCIATED CONTENT

Supporting Information

The Supporting Information is available free of charge at https://pubs.acs.org/doi/10.1021/acsaem.5c02284.

Surface elemental ratios determined via XPS, ellipsometry data, EIS data, 3D ToF-SIMS data, and AFM surface profile (PDF)

■ AUTHOR INFORMATION

Corresponding Author

Alexander J. E. Rettie − *Electrochemical Innovation Lab, Department of Chemical Engineering, University College London, London WC1E 6DH, U.K.; Advanced Propulsion Lab, University College London, Stratford E20 2AE, U.K.;* orcid.org/0000-0002-2482-9732; Email: a.rettie@ucl.ac.uk

Authors

Thomas E. Gill − *Electrochemical Innovation Lab, Department of Chemical Engineering, University College London, London WC1E 6DH, U.K.; Advanced Propulsion Lab, University College London, Stratford E20 2AE, U.K.;* orcid.org/0000-0002-0231-9627

Guillaume Matthews − *Department of Materials, University of Oxford, Oxford OX1 3PH, U.K.;* orcid.org/0000-0002-6352-8596

Yaoguang Song − *Electrochemical Innovation Lab, Department of Chemical Engineering, University College London, London WC1E 6DH, U.K.; Advanced Propulsion Lab, University College London, Stratford E20 2AE, U.K.*

Mo El Maoued − *Manufacturing Futures Lab, Department of Chemical Engineering, University College London, London WC1E 6DH, U.K.*

Adam J. Lovett − *Electrochemical Innovation Lab, Department of Chemical Engineering, University College London, London WC1E 6DH, U.K.; Advanced Propulsion Lab, University College London, Stratford E20 2AE, U.K.;* orcid.org/0000-0002-3076-2992

Sadia Sheraz − *Department of Chemistry, Photon Science Institute, The University of Manchester, Manchester M13 9PL, U.K.*

Nicholas P. Lockyer − *Department of Chemistry, Photon Science Institute, The University of Manchester, Manchester M13 9PL, U.K.;* orcid.org/0000-0002-9674-9395

Amita Ummadisingu − *Manufacturing Futures Lab, Department of Chemical Engineering, University College London, London WC1E 6DH, U.K.*

Thomas S. Miller − *Electrochemical Innovation Lab, Department of Chemical Engineering, University College London, London WC1E 6DH, U.K.; Advanced Propulsion Lab, University College London, Stratford E20 2AE, U.K.;* orcid.org/0000-0002-2224-5768

Complete contact information is available at: https://pubs.acs.org/10.1021/acsaem.5c02284

Author Contributions

The manuscript was written through contributions of all authors. All authors have given approval to the final version of the manuscript.

Notes

The authors declare no competing financial interest.

■ ACKNOWLEDGMENTS

We gratefully acknowledge EPSRC New Investigator award (EP/W029235/1), IAA Discovery-to-use grant (EP/X525649/1) and a DTP Studentship for T.E.G.: EP/R513143/1, EP/T517793/1. T.S.M. and A.J.L. acknowledge the Faraday Battery Challenge through the High Silicon Content Anodes for a Solid State Battery project (HISTORY, project number: 10040711). T.S.M. and A.J.E.R. acknowledge the Lithium Sulfur Technology Accelerator (LiSTAr) program (EP/S003053/1, Grant FIRG014, FIRG058, FIRG083) and T.S.M. acknowledges the Faraday Institution through Nextrode program (EP/S003053/1, Grant FIRG066). A.U. thanks the Royal Society grant no. RGS\R2\242537. The ToF-SIMS studies were supported by the Henry Royce Institute for Advanced Materials, funded through EPSRC grants EP/R00661X/1, EP/S019367/1, EP/P025021/1 and EP/P025498/1. Finally, we thank M. Furedi and S. Guldin for access to the ellipsometer.

■ REFERENCES

(1) Lee, B.; Paek, E.; Mitlin, D.; Lee, S. W. Sodium Metal Anodes: Emerging Solutions to Dendrite Growth. *Chem. Rev.* **2019**, *119*, 5416.

(2) Huang, J.; Wu, K.; Xu, G.; Wu, M.; Dou, S.; Wu, C. Recent Progress and Strategic Perspectives of Inorganic Solid Electrolytes: Fundamentals, Modifications, and Applications in Sodium Metal Batteries. *Chem. Soc. Rev.* **2023**, *52* (15), 4933−4995.

(3) Liu, G.; Yang, J.; Wu, J.; Peng, Z.; Yao, X. Inorganic Sodium Solid Electrolytes: Structure Design, Interface Engineering and Application. *Adv. Mater.* **2024**, *36*, 2311475.

(4) Tsai, C. L.; Lan, T.; Dellen, C.; Ling, Y.; Ma, Q.; Fattakhova-Rohlfing, D.; Guillon, O.; Tietz, F. Dendrite-Tolerant All-Solid-State Sodium Batteries and an Important Mechanism of Metal Self-Diffusion. *J. Power Sources* **2020**, *476* (August), 228666.

(5) Fu, H.; Yin, Q.; Huang, Y.; Sun, H.; Chen, Y.; Zhang, R.; Yu, Q.; Gu, L.; Duan, J.; Luo, W. Reducing Interfacial Resistance by Na-SiO2 Composite Anode for NASICON-Based Solid-State Sodium Battery. *ACS Mater. Lett.* **2020**, *2* (2), 127−132.

(6) Zhou, W.; Li, Y.; Xin, S.; Goodenough, J. B. Rechargeable Sodium All-Solid-State Battery. *ACS Cent. Sci.* **2017**, *3* (1), 52−57.

(7) Miao, X.; Di, H.; Ge, X.; Zhao, D.; Wang, P.; Wang, R.; Wang, C.; Yin, L. AlF3-Modified Anode-Electrolyte Interface for Effective Na Dendrites Restriction in NASICON-Based Solid-State Electrolyte. *Energy Storage Mater.* **2020**, *30* (May), 170−178.

(8) Bay, M. C.; Wang, M.; Grissa, R.; Heinz, M. V. F.; Sakamoto, J.; Battaglia, C. Sodium Plating from Na-β''-Alumina Ceramics at Room Temperature, Paving the Way for Fast-Charging All-Solid-State Batteries. *Adv. Energy Mater.* **2020**, *10* (3), 1−8.

(9) Li, J.; Ma, C.; Chi, M.; Liang, C.; Dudney, N. J. Solid Electrolyte: The Key for High-Voltage Lithium Batteries. *Adv. Energy Mater.* **2015**, *5* (4), 1−6.

(10) Bates, J. B.; Dudney, N. J.; Neudecker, B.; Ueda, A.; Evans, C. D.; ThinBates, J. B.; Dudney, N. J.; Neudecker, B.; Ueda, A.; Evans,

C. D. Thin-Film Lithium and Lithium-Ion Batteries. *Solid State Ionics* **2000**, *135* (1−4), 33−45.
(11) Han, F.; Westover, A. S.; Yue, J.; Fan, X.; Wang, F.; Chi, M.; Leonard, D. N.; Dudney, N. J.; Wang, H.; Wang, C. High Electronic Conductivity as the Origin of Lithium Dendrite Formation within Solid Electrolytes. *Nat. Energy* **2019**, *4* (3), 187−196.
(12) Krauskopf, T.; Richter, F. H.; Zeier, W. G.; Janek, J. Physicochemical Concepts of the Lithium Metal Anode in Solid-State Batteries. *Chem. Rev.* **2020**, *120* (15), 7745−7794.
(13) Cheng, D.; Wynn, T. A.; Wang, X.; Wang, S.; Zhang, M.; Shimizu, R.; Bai, S.; Nguyen, H.; Fang, C.; KimLi, M. W.; Lu, B.; Kim, S. J.; Meng, Y. S.; Meng, Y. S. Unveiling the Stable Nature of the Solid Electrolyte Interphase between Lithium Metal and LiPON via Cryogenic Electron Microscopy. *Joule* **2020**, *4* (11), 2484−2500.
(14) Su, J.; Pasta, M.; Ning, Z.; Gao, X.; Bruce, P. G.; Grovenor, C. R. M. Interfacial Modification between Argyrodite-Type Solid-State Electrolytes and Li Metal Anodes Using LiPON Interlayers. *Energy Environ. Sci.* **2022**, *15* (9), 3805−3814.
(15) Lee, S.; Jung, S.; Yang, S.; Lee, J. H.; Shin, H.; Kim, J.; Park, S. Revisiting the LiPON/Li Thin Film as a Bifunctional Interlayer for NASICON Solid Electrolyte-Based Lithium Metal Batteries. *Appl. Surf. Sci.* **2022**, *586* (November 2021), 152790.
(16) Liu, W.; Guo, R.; Zhan, B.; Shi, B.; Li, Y.; Pei, H.; Wang, Y.; Shi, W.; Fu, Z.; Xie, J. Artificial Solid Electrolyte Interphase Layer for Lithium Metal Anode in High-Energy Lithium Secondary Pouch Cells. *ACS Appl. Energy Mater.* **2018**, *1* (4), 1674−1679.
(17) Wang, W.; Yue, X.; Meng, J.; Wang, J.; Wang, X.; Chen, H.; Shi, D.; Fu, J.; Zhou, Y.; Chen, J.; Fu, Z. Lithium Phosphorus Oxynitride as an Efficient Protective Layer on Lithium Metal Anodes for Advanced Lithium-Sulfur Batteries. *Energy Storage Mater.* **2019**, *18* (August 2018), 414−422.
(18) Nuwayhid, R. B.; Jarry, A.; Rubloff, G. W.; Gregorczyk, K. E. Atomic Layer Deposition of Sodium Phosphorus Oxynitride: A Conformal Solid-State Sodium-Ion Conductor. *ACS Appl. Mater. Interfaces* **2020**, *12* (19), 21641−21650.
(19) Nuwayhid, R. B.; Fontecha, D.; Kozen, A. C.; Jarry, A.; Lee, S. B.; Rubloff, G. W.; Gregorczyk, K. E. Nanoscale Li, Na, and K Ion-Conducting Polyphosphazenes by Atomic Layer Deposition. *Dalton Trans.* **2022**, *51* (5), 2068−2082.
(20) Nuwayhid, R. B.; Kozen, A. C.; Long, D. M.; Ahuja, K.; Rubloff, G. W.; Gregorczyk, K. E. Dynamic Electrode-Electrolyte Intermixing in Solid-State Sodium Nano-Batteries. *ACS Appl. Mater. Interfaces* **2023**, *15* (20), 24271−24283.
(21) Clayton, D. R.; Lepage, D.; Plassmeyer, P. N.; Page, C. J.; Lonergan, M. C. Low-Temperature Fabrication of Lithium Aluminum Oxide Phosphate Solid Electrolyte Thin Films from Aqueous Precursors. *RSC Adv.* **2017**, *7* (12), 7046−7051.
(22) Vadhva, P.; Gill, T. E.; Cruddos, J. H.; Said, S.; Siniscalchi, M.; Narayanan, S.; Pasta, M.; Miller, T. S.; Rettie, A. J. E. Engineering Solution-Processed Non-Crystalline Solid Electrolytes for Li Metal Batteries. *Chem. Mater.* **2023**, *35* (3), 1168−1176.
(23) Zhang, Z.; Smith, K.; Jervis, R.; Shearing, P. R.; Miller, T. S.; Brett, D. J. L. Operando Electrochemical Atomic Force Microscopy of Solid-Electrolyte Interphase Formation on Graphite Anodes: The Evolution of SEI Morphology and Mechanical Properties. *ACS Appl. Mater. Interfaces* **2020**, *12* (31), 35132−35141.
(24) Zhang, Z.; Said, S.; Lovett, A. J.; Jervis, R.; Shearing, P. R.; Brett, D. J. L.; Miller, T. S. The Influence of Cathode Degradation Products on the Anode Interface in Lithium-Ion Batteries. *ACS Nano* **2024**, *18* (13), 9389−9402.
(25) Said, S.; Zhang, Z.; Shutt, R. R. C.; Lancaster, H. J.; Brett, D. J. L.; Howard, C. A.; Miller, T. S. Black Phosphorus Degradation during Intercalation and Alloying in Batteries. *ACS Nano* **2023**, *17* (7), 6220−6233.
(26) Nečas, D.; Klapetek, P. Gwyddion: An Open-Source Software for SPM Data Analysis. *Cent. Eur. J. Phys.* **2012**, *10* (1), 181−188.
(27) Fletcher, J. S.; Rabbani, S.; Henderson, A.; Blenkinsopp, P.; Thompson, S. P.; Lockyer, N. P.; Vickerman, J. C. A New Dynamic in Mass Spectral Imaging of Single Biological Cells. *Anal. Chem.* **2008**, *80* (23), 9058−9064.
(28) Randau, S.; Weber, D. A.; Kötz, O.; Koerver, R.; Braun, P.; Weber, A.; Ivers-Tiffée, E.; Adermann, T.; Kulisch, J.; Zeier, W. G.; Richter, F. H.; Janek, J. Benchmarking the Performance of All-Solid-State Lithium Batteries. *Nat. Energy* **2020**, *5* (3), 259−270.
(29) Lasia, A. *Electrochemical Impedance Spectroscopy and Its Applications*; Springer New York, NY, 2014; pp 1−367.
(30) Westerhoff, U.; Kurbach, K.; Lienesch, F.; Kurrat, M. Analysis of Lithium-Ion Battery Models Based on Electrochemical Impedance Spectroscopy. *Energy Technol.* **2016**, *4* (12), 1620−1630.
(31) Meyers, S. T.; Anderson, J. T.; Hong, D.; Hung, C. M.; Wager, J. F.; Keszler, D. A. Solution-Processed Aluminum Oxide Phosphate Thin-Film Dielectrics. *Chem. Mater.* **2007**, *19* (16), 4023−4029.
(32) Yuvaraj, S.; Fan-Yuan, L.; Tsong-Huei, C.; Chuin-Tih, Y. Thermal Decomposition of Metal Nitrates in Air and Hydrogen Environments. *J. Phys. Chem. B* **2003**, *107* (4), 1044−1047.
(33) Herbert, E. G.; Tenhaeff, W. E.; Dudney, N. J.; Pharr, G. M. Mechanical Characterization of LiPON Films Using Nanoindentation. *Thin Solid Films* **2011**, *520* (1), 413−418.
(34) Yu, S.; Schmidt, R. D.; Garcia-Mendez, R.; Herbert, E.; Dudney, N. J.; Wolfenstine, J. B.; Sakamoto, J.; Siegel, D. J. Elastic Properties of the Solid Electrolyte Li7La3Zr2O12 (LLZO). *Chem. Mater.* **2016**, *28* (1), 197−206.
(35) Kato, A.; Nagao, M.; Sakuda, A.; Hayashi, A.; Tatsumisago, M. Evaluation of Young's Modulus of Li2S-P2S 5-P2O5 Oxysulfide Glass Solid Electrolytes. *J. Ceram. Soc. Jpn.* **2014**, *122* (1427), 552−555.
(36) Hayashi, A.; Sakuda, A.; Tatsumisago, M. Development of Sulfide Solid Electrolytes and Interface Formation Processes for Bulk-Type All-Solid-State Li and Na Batteries. *Front. Energy Res.* **2016**, *4* (JUL), 1−13.
(37) Keshri, S. R.; Ganisetti, S.; Kumar, R.; Gaddam, A.; Illath, K.; Ajithkumar, T. G.; Balaji, S.; Annapurna, K.; Nasani, N.; Krishnan, N. M. A.; Allu, A. R. Ionic Conductivity of Na3Al2P3O12Glass Electrolytes - Role of Charge Compensators. *Inorg. Chem.* **2021**, *60* (17), 12893−12905.
(38) Barik, S. K.; Senapati, A.; Chakraborty, S.; Ananthasivan, K. Structure and Optical Properties of Sodium Aluminium Phosphate Glass Matrix Containing Lanthanide Oxides (Ce, Pr, Nd and Gd). *J. Inorg. Organomet. Polym. Mater.* **2023**, *33* (7), 2093−2110.
(39) Balabinskaya, A. S.; Ivanova, E. N.; Ivanova, M. S.; Kumzerov, Y. A.; Pan'Kova, S. V.; Poborchii, V. V.; Romanov, S. G.; Solovyev, V. G.; Khanin, S. D. Investigation into the Electrical and Optical Properties of Sodium Nitrite and Sodium Nitrate Nanoparticles in Regular Porous Matrices. *Glass Phys. Chem.* **2005**, *31* (3), 330−336.
(40) Dudney, N. J. Composite Electrolytes. *Annu. Rev. Mater. Sci.* **1989**, *19*, 103−120.
(41) Lacivita, V.; Artrith, N.; Ceder, G. Structural and Compositional Factors That Control the Li-Ion Conductivity in LiPON Electrolytes. *Chem. Mater.* **2018**, *30* (20), 7077−7090.

https://doi.org/10.1021/acsaem.5c02284
ACS Appl. Energy Mater. 2025, 8, 14592−14600